



Enhanced liver X receptor signalling reduces brain injury and promotes tissue regeneration following experimental intracerebral haemorrhage: roles of microglia/macrophages

Ruiyi Zhang ^{1,2,3}, Yifei Dong,⁴ Yang Liu,^{1,2} Dorsa Moezzi,³ Samira Ghorbani,³ Reza Mirzaei,³ Brian M Lozinski,³ Jeff F Dunn,⁵ V Wee Yong,³ Mengzhou Xue ^{1,2}

To cite: Zhang R, Dong Y, Liu Y, *et al.* Enhanced liver X receptor signalling reduces brain injury and promotes tissue regeneration following experimental intracerebral haemorrhage: roles of microglia/macrophages. *Stroke & Vascular Neurology* 2023;**8**: e002331. doi:10.1136/svn-2023-002331

► Additional supplemental material is published online only. To view, please visit the journal online (<http://dx.doi.org/10.1136/svn-2023-002331>).

VWY and MX are joint senior authors.

Received 20 January 2023
Accepted 20 April 2023
Published Online First
3 May 2023



© Author(s) (or their employer(s)) 2023. Re-use permitted under CC BY-NC. No commercial re-use. See rights and permissions. Published by BMJ.

For numbered affiliations see end of article.

Correspondence to

Professor V Wee Yong;
vyong@ucalgary.ca

Professor Mengzhou Xue;
xuemengzhou@zzu.edu.cn

ABSTRACT

Background Inflammation-exacerbated secondary brain injury and limited tissue regeneration are barriers to favourable prognosis after intracerebral haemorrhage (ICH). As a regulator of inflammation and lipid metabolism, Liver X receptor (LXR) has the potential to alter microglia/macrophage (M/M) phenotype, and assist tissue repair by promoting cholesterol efflux and recycling from phagocytes. To support potential clinical translation, the benefits of enhanced LXR signalling are examined in experimental ICH.

Methods Collagenase-induced ICH mice were treated with the LXR agonist GW3965 or vehicle. Behavioural tests were conducted at multiple time points. Lesion and haematoma volume, and other brain parameters were assessed using multimodal MRI with T2-weighted, diffusion tensor imaging and dynamic contrast-enhanced MRI sequences. The fixed brain cryosections were stained and confocal microscopy was applied to detect LXR downstream genes, M/M phenotype, lipid/cholesterol-laden phagocytes, oligodendrocyte lineage cells and neural stem cells. Western blot and real-time qPCR were also used. CX3CR1^{CreER}; Rosa26^{IDTR} mice were employed for M/M-depletion experiments.

Results GW3965 treatment reduced lesion volume and white matter injury, and promoted haematoma clearance. Treated mice upregulated LXR downstream genes including ABCA1 and Apolipoprotein E, and had reduced density of M/M that apparently shifted from proinflammatory interleukin-1 β ⁺ to Arginase1⁺CD206⁺ regulatory phenotype. Fewer cholesterol crystal or myelin debris-laden phagocytes were observed in GW3965 mice. LXR activation increased the number of Olig2⁺PDGFR α ⁺ precursors and Olig2⁺CC1⁺ mature oligodendrocytes in perihematoma regions, and elevated SOX2⁺ or nestin⁺ neural stem cells in lesion and subventricular zone. MRI results supported better lesion recovery by GW3965, and this was corroborated by return to pre-ICH values of functional rotarod activity. The therapeutic effects of GW3965 were abrogated by M/M depletion in CX3CR1^{CreER}; Rosa26^{IDTR} mice.

Conclusions LXR agonism using GW3965 reduced brain injury, promoted beneficial properties of M/M and facilitated tissue repair correspondent with enhanced cholesterol recycling.

WHAT IS ALREADY KNOWN ON THIS TOPIC

⇒ In a previous study, another synthetic Liver X receptor (LXR) agonist, T0901317, was reported to inhibit proinflammatory molecules in the early phase after collagenase induced intracerebral haemorrhage (ICH). However, whether the enhanced LXR signalling promoted microglia/macrophage (M/M) phenotype shifting, cholesterol recycling and tissue regeneration remains unknown.

WHAT THIS STUDY ADDS

⇒ We observed an apparent M/M phenotype shift and reduced lipid burden associated with alleviated brain injury and tissue regeneration by LXR agonism after ICH; the intact M/M cluster appears indispensable to the therapeutic effects of GW3965.

HOW THIS STUDY MIGHT AFFECT RESEARCH, PRACTICE OR POLICY

⇒ The neuroprotective and regenerative benefits of short-term LXR agonism demonstrated in this study make them promising for use in clinical ICH.

INTRODUCTION

Intracerebral haemorrhage (ICH) accounts for 12%–20% of all types of stroke with over 2 million individuals worldwide being afflicted annually.¹ Even with the development of minimally invasive surgical processes, the prognosis of ICH is catastrophic.² The latter is attributed to inflammation-mediated secondary brain injury and limited tissue regeneration.^{3–4} CNS-resident microglia and infiltrating monocyte-derived macrophages are at the nexus of inflammation and regeneration.⁵ From postmortem studies, the density of microglia/macrophages (M/M) elevates in the perihematoma region from the first day of ICH and increases thereafter.⁶ The transcriptome of haematoma-associated myeloid cells may shift temporally from proinflammatory to phagocytic, anti-inflammatory

and antioxidative.⁷ Preclinical data show that inhibiting microglia activation or macrophage infiltration in the early phases after experimental ICH reduces secondary brain injury,^{8–10} while longterm inhibition impairs tissue regeneration and recovery, presumably due to insufficient beneficial M/M at later stages.^{5 11 12} Thus, it would be ideal to inhibit the proinflammatory/injurious properties of M/M and promote their regulatory and reparative properties following ICH. One such candidate could be the elevation of Liver X receptor (LXR) signalling.

LXR α or β nuclear receptors form heterodimers with retinoid X receptor (RXR), where the complex then binds to a specific DNA region containing repetitive AGGTCA sequence named LXR response element.^{13 14} When ligands are absent, the LXR-RXR complex binds to a corepressor such as histone deacetylase 3, silencing mediator for retinoid and thyroid receptors, or nuclear receptor corepressor to remain inactivated, thereby preventing the transcription of downstream genes including apolipoprotein E (ApoE), ATP-binding cassette transporter subfamily A and G (ABCA, ABCG), and inducible degrader of LDLR.^{15–18} When endogenous (eg, cholesterol derivatives or cholic acid) or synthetic ligands (eg, GW3965 and T0901317) bind LXRs, the LXR-RXR heterodimer changes conformation and releases corepressors while recruiting coactivators such as histone acetyltransferase p300 and activating signal co-integrator 2.^{19–25} The latter sequentially induces the expression of target genes to facilitate cholesterol efflux and lipid metabolism.²⁶

Because the cholesterol within the adult CNS mainly relies on de novo synthesis in physiological condition,²⁷ neural cells including neural stem cells (NSCs) and oligodendrocyte progenitor cells can only use recycled cholesterol after an acute injury due to insufficient synthesis, and thus may be vulnerable to cholesterol deficiency. As the main processors of cholesterol-rich myelin and cellular components, M/M could degrade these debris and recycle the cholesterol for repair. If so, upregulated LXR signalling could promote cholesterol efflux from phagocytes to facilitate tissue regeneration.^{28–30} Additionally, ligand bonded LXRs can be SUMOylated to interact with nuclear factor kappa B, activator protein 1 (AP-1) and signal transducer and activator of transcription 1, leading to the transrepression of their downstream proinflammatory genes.^{31–33} Moreover, analyses by transposase-accessible chromatin sequencing and chromatin immunoprecipitation sequencing show that activated LXRs could bind inflammatory gene enhancers to induce chromatin closing, resulting in cis-repression of these genes in lipopolysaccharide-treated bone marrow derived macrophages.³⁴

Given the requirement for cholesterol recycling for lipid synthesis in regenerating oligodendrocytes and myelin,^{29 30} and the importance of preventing excessive neuroinflammation, stimulating the LXR pathway may have therapeutic benefits in ICH through neuroprotection in the acute period, and in regenerative processes in

the longer term. In this manuscript, we evaluated the therapeutic effects and potential mechanisms of LXR stimulation following ICH for neuroprotection and reparative oligodendrocyte repopulation.

METHODS

The data that support the findings of this study are available from the corresponding authors on reasonable request.

Animals

Animals were sacrificed when they showed any signs of distress: inability to properly drink, eat, groom themselves, unresponsiveness, isolation, seizures or when there was unexpected loss of body weight (higher than 20%, relative to the starting weight of the animal and controls). Male C57Bl/6J mice acquired from Charles River (Montreal) were used at 8–12 weeks of age for in vivo experiments and were housed in individual ventilated cages with 22°C–24°C temperature, 50%–60% humidity, environmental enrichment and free access to food and water. Eighty-eight C57Bl/6J mice were randomly assigned to 6 groups including sham (n=9), ICH (n=15), sham+DMSO (n=6), sham+GW3965 (n=6), ICH+DMSO (n=24) and ICH+GW3965 (n=24). Two mice that died immediately after surgery and 2 other mice that did not have anticipated behavioural deterioration (less than 20% drop 1 day after surgery compared with baseline of either behavioural test) after experimental ICH were excluded according to preset criteria.

CX3CR1^{CreER} (JAX 021160) mice and Rosa26^{IDTR} (JAX 007900) mice from The Jackson Laboratory were bred in the single mouse barrier unit at the University of Calgary to produce CX3CR1^{CreER}:Rosa26^{IDTR} mice. On tamoxifen treatment to induce the diphtheria toxin (DT) receptor on CX3CR1-expressing cells (mostly M/M), the subsequent administration of DT would kill M/M. Male mice were used in the M/M-conditional depletion experiments at the age of 12–20 weeks. Tamoxifen (75 mg/kg, T5648, Sigma) dissolved in corn oil (Sigma, C8267) was given intraperitoneally (IP) once a day for five consecutive days. Three days after the last injection, and corresponding to the day of ICH surgery, DT (50 μ g/kg) or saline was injected IP, followed by daily DT or saline for the next 6 days to ensure the depletion of M/M. Moreover, 1 hour after ICH, randomly assigned mice were initiated daily IP of GW3965 or vehicle (50% DMSO). In this manner, 24 CX3CR1^{CreER}:Rosa26^{IDTR} mice that were subjected to ICH were in four groups of saline+DMSO (n=4), saline+GW3965 (n=4), DT+DMSO (n=8) and DT+GW3965 (n=7, one mice died 6 days after surgery).

Collagenase-induced ICH

The procedure for collagenase-induced ICH in mice is described in previous studies,³⁵ and was approved by Animal Care Committee of the University of Calgary. Briefly, mice were anaesthetised with IP injection of ketamine (100 mg/kg) and xylazine (10 mg/kg). Fur

was removed from the surgical site using hair clippers. Ophthalmic gel was applied to both eyes to keep them moist throughout the surgery and recovery period. A heat lamp was used over the stereotaxic frame to provide heat support to the animal during the procedure. The mouse was placed in a stereotaxic frame using modified ear bars fitted with blunt rubber ends designed for mice. The surgical site was cleaned using betadine and a skin incision was made to reveal the skull. An area of the skull above the right striatum was located according to the following coordinates (2.0 mm lateral and 0.8 mm anterior to the bregma), and a 0.5 mm cranial burr hole was made with a microdrill. A Hamilton syringe, containing 0.05 U of collagenase type VII dissolved in 0.5 μ L of saline was lowered through the hole until 3.2 mm beneath the skull, ending in the striatum. The injection of collagenase lasted for 5 min per mouse and was controlled by a UMP3 UltraMicroPump. Following injection, the needle was maintained inside the brain for another 5 min to prevent reflux. The needle was then slowly withdrawn. Finally, the surgical site was sutured and disinfected. Animals were transferred into a warm incubator chamber at approximately 32°C until full recovery. Mice were then returned to their cages, given free access to food and water and monitored daily. For sham animals, the same volume of saline (0.5 μ L) without collagenase was injected following the same procedure.

GW3965 treatment

For LXR activation *in vivo*, mice were injected once daily, IP with sterile 50% DMSO (Sigma) or 50% DMSO containing the LXR agonist GW3965 (Sigma) at 10 mg/kg.^{36 37} Treatment started 1 hour after intracerebral collagenase injection, and then once daily until day 7 (7 doses in total). Mice were randomly numbered before surgical procedure and odd numbers were assigned to DMSO control group while even numbers were assigned to GW3965 treatment group. Injection was conducted alternately between the two groups, and each cage included mice from both groups.

Brain tissue isolation

Mice were euthanised with a ketamine and xylazine overdose at 1, 3, 7 or 14 days postsurgery. A total of 15 mL of PBS was then perfused via cardiac puncture, followed by perfusion with 15 mL of 4% paraformaldehyde (PFA) in PBS. The whole brain was then dissected from the skull of the mouse and left in 4% PFA in PBS for fixation. After overnight fixation in 4% PFA at 4°C, brain samples were transferred to 30% sucrose solution for dehydration. After at least 48 hours of incubation in 30% sucrose solution, the cerebellum was removed and the remaining brain tissue was frozen in FSC 22 frozen section media (Leica). Using a cryostat (ThermoFisher Scientific), brain tissue was cut coronally into

20 μ m sections, collected onto Superfrost Plus microscope slides (VWR) and stored at -20°C before analysis.

Antibodies and fluorescent dyes

The following primary antibodies were used for immunofluorescence microscopy (stock concentrations were not informed by some suppliers): chicken anti-mouse glial fibrillar acidic protein (GFAP) (1:1000; BioLegend, 829401); rabbit anti-human/mouse Iba1 (1:1000 of 0.6 mg/mL stock; Wako, 019-19741); rabbit anti-human/mouse NeuN (1:500 of 0.82 mg/mL stock; Abcam, ab177487); rat anti-mouse CD68 (1:500 of 0.5 mg/mL stock; BioLegend, 137002); goat anti-human/mouse Olig2 (1:200 of 0.2 mg/mL stock; R&D Systems, AF2418); chicken anti-human/mouse myelin basic protein (MBP) (1:2000; ThermoFisher, PA1-10008); rabbit anti-human/mouse neurofilament heavy chain (NF-H) (1:1000 of 1 mg/mL stock; Encor Biotechnology, RPCA-NF-H); rat anti-mouse ATP Binding Cassette Subfamily A Member 1 (ABCA1) (1:200; ThermoFisher, MA1-16936); rabbit anti-human/mouse ApoE (1:500 of 0.5 mg/mL stock; ThermoFisher, 701241); goat anti-mouse interleukin (IL)-1 β (1:50 of 0.2 mg/mL stock; R&D Systems, AF-401-NA); rat anti-mouse inducible nitric oxide synthase (iNOS) (1:100 of 0.5 mg/mL stock; ThermoFisher, 14-5920-82); rabbit anti-mouse arginase (Arg1) (1:200 of 18 μ g/mL stock; Cell Signaling, 93668S); goat anti-mouse CD206 (1:200 of 0.2 mg/mL stock; ThermoFisher, PA5-46994); rabbit anti-human/mouse Olig2 (1:200; Millipore, AB9610); goat anti-mouse platelet-derived growth factor receptor (PDGFR) α (1:200 of 0.2 mg/mL stock; R&D Systems, AF1062); mouse anti-human/mouse adenomatous polyposis coli (APC), clone CC-1 (1:200 of 0.1 mg/mL stock; Millipore, OP80-100UG); rabbit anti-human/mouse amyloid precursor protein (APP) (1:500 of 0.25 mg/mL stock; ThermoFisher, 36-6900); rat anti-human/mouse SOX2 (1:200 of 0.5 mg/mL stock; ThermoFisher, 14-9811-82); chicken anti-human/mouse nestin (1:1000 of 0.3 mg/mL stock; Novusbio, NB100-1604); rabbit anti-human/mouse Ki67 (1:500 of 0.8 mg/mL stock; Abcam, ab15580); rabbit anti-mouse doublecortin (DCX) (1:800 of 130 μ g/mL; Cell Signaling, 4604) and rat anti-mouse CD16/CD32 Fc blocking antibody (1:100 of 0.5 mg/mL stock; BD Biosciences, 553142).

The following secondary antibodies from Jackson ImmunoResearch were used at 1:400 dilution of 0.625 mg/mL stock: Alexa Fluor 488 donkey anti-mouse IgG, Alexa Fluor 488 donkey anti-rat IgG, Alexa Fluor 488 donkey anti-chicken IgY, cyanine Cy3 donkey anti-goat IgG, cyanine Cy3 donkey anti-chicken IgY, Alexa Fluor 594 donkey anti-chicken IgY, and Alexa Fluor 647 donkey anti-rabbit IgG.

These fluorescent dyes were used to counterstain with antibodies for immunofluorescence microscopy: DAPI (1:1000 of 1 mg/mL stock; Sigma, D9542-10MG); BODIPY 493/503 (1:1500 of 1 mg/mL stock; ThermoFisher, D3922); and FluoroMyelin Green Fluorescent Myelin Stain (1:300; ThermoFisher, F34651).

Immunofluorescence staining

Microscope slides containing mouse brain samples were warmed to room temperature (RT) for 30 min. For MBP staining, slides were also delipidated by successive washes of 50%, 70%, 90%, 95%, 100%, 100%, 95%, 90%, 70% and 50% ethanol. Sections were then rehydrated with PBS for 10 min, and permeabilised with 0.2% Triton X-100 in PBS 10 min. Horse blocking solution (PBS, 10% horse serum, 1% BSA, 0.1% cold water fish skin gelatin, 0.1% Triton X-100, 0.05% Tween-20) was used to block the sample for 1 hour at RT. Alternatively, for staining using the CC1 antibody in mouse sections, purified rat anti-mouse CD16/CD32 Fc blocking antibody (1:100 of 0.5 mg/mL stock; BD Biosciences, 553142) was added to the blocking buffer. After blocking, samples were incubated with primary antibodies resuspended in antibody dilution buffer (PBS, 1% BSA, 0.1% cold water fish skin gelatin, 0.1% Triton X-100) overnight at 4°C. Following this, samples were washed three times, 5 min each, using PBS with 0.2% Tween-20, and then incubated with secondary antibodies (and FluoroMyelin or Bodipy for specific staining) and DAPI resuspended in the antibody dilution buffer for 1 hour at RT. The samples were then washed three more times using PBS with 0.2% Tween-20, 5 min each, and the coverslips were mounted onto the slides using Fluoromount-G solution (SouthernBiotech).

Confocal immunofluorescence microscopy

Laser confocal immunofluorescence images were acquired at RT using the Leica TCS Sp8 laser-scanning confocal microscope, using $\times 25/0.5$ NA water objective for all samples and experiments. The 405 nm, 488 nm, 552 nm and 640 nm lasers were used to excite the fluorophores from antibodies and fluorescent dyes bound to samples and detected by two low-dark-current Hamamatsu PMT detectors and two high-sensitivity hybrid detectors on the Sp8. Multiple-FOV images of perihæmatomal regions were acquired using the following parameters: in 8 bits, in a z-stack with one-directional scanning, 1 airy unit pinhole, $\times 0.75$ zoom, $0.57 \mu\text{m}$ per optical section, and 2048×2048 pixels x–y resolution. For reflection microscopy, reflection of crystals was captured by placing a PMT detector directly over the 552 nm laser channel for reflection light capture, and fluorescence was simultaneously captured by the same confocal imaging techniques.^{30 38–40} For whole-lesion tile scan, zoom factor was adjusted to 1.3 to diminish shades between images, and all other parameters were kept the same. Equal laser, gain and offset settings to maximise contrast and minimise saturation were consistently used for all samples within each set of experiments. A sample slide stained with only the secondary antibodies and DAPI was always included for each experiment as a control to account for non-specific secondary immunofluorescence. Tile scan of the whole lesion or images from four FOV of the perihæmatomal region of two lesion epicentres were acquired and averaged per biological replicate for analysis. Leica Application Suite X was used for image acquisition,

ImageJ was used for image threshold and particle analysis, and Imaris was used for three-dimensional (3D) rendering.

The overview of brain section at different time points after surgery was imaged using Olympus vs120 slide scanner by a $20\times$ objective with same laser and exposure settings. Images were extracted using OlyVIA (Olympus), and only the brightness and contrast were adjusted for better display.

Confocal image analysis

The z-stacks of confocal images were analysed using ImageJ. For each image z-stack, maximum-intensity projections were created with pseudocolor for each channel/marker from .lif file and analysed under eight-bit format. Then, an ROI was drawn around the lesion or perihæmatomal region according to GFAP, Iba1, CD68 or nestin staining, and the area outside the ROI was excluded for analysis. To determine the positive signal, the threshold was set consistently using a value determined using the negative secondary antibody-stained control, contralateral and sham control. The analyse particles function was then used to create a mask and to quantify the positive signals in each ROI. The same brightness threshold values for setting the positive signal, as well as the size and circularity settings for particle analysis, were used consistently across all samples for each experimental set. For the representative images shown, the maximum-intensity projection of each channel/marker in a z-stack was merged and converted to RGB format by ImageJ. Only the brightness and contrast settings were adjusted, and consistently among samples, to better display the images. A 3D rendering of confocal image z-stacks was created in Imaris (Oxford Instrument) using the surface creation tool with background subtraction and machine learning-based signal filtration.

Quantitative real-time PCR

Total RNA was isolated from perihæmatomal regions using RNeasy Mini kit (Qiagen) according to the manufacturer's instructions and stored at -80°C . The concentration and purity of RNA were determined by measuring absorbance at 260/280 nm using a nanodrop spectrophotometer (Thermo Fisher Scientific). First strand cDNA synthesis was performed with $1 \mu\text{g}$ total RNA using miScript II RT Kit (Qiagen) for mRNA expression analyses according to the manufacturer's instructions. Real-time qPCR was performed using QuantiFast SYBR Green master mix (Qiagen) and Quantitect Primers: ABCA1 (Qiagen, QT00165690), ApoE (Qiagen, QT01043889) and Actb (Qiagen, QT00095242) with the following cycling conditions: 95°C for 5 min, 40 cycles of denaturation at 95°C for 30 s, annealing at 60°C for 30 s and extension at 72°C for 30 s. Beta-actin housekeeping genes were used to normalise mRNA expression. The relative expression levels were analysed by $2^{-\Delta\Delta\text{Ct}}$ method.

Western blotting

Tissue extracts of perihematoma regions were generated by RIPA Buffer (Sigma, R0278) supplemented with protease inhibitor cocktail (Sigma, P2714). Protein concentrations were determined using a bicinchoninic acid (BCA) assay kit (Sigma) with BSA as standard. Equal amounts of total protein and 10 μ L of PageRuler Plus Prestained Protein Ladder (Thermo Fisher) were then run on NuPAGE Bis-Tris Protein Gels (Thermo Fisher) with Mops SDS Running Buffer (Thermo Fisher). After transferring to Hybond polyvinylidene difluoride (Amersham) membrane using a wet transfer system (Bio-Rad), membranes were blocked with 5% BSA and then probed overnight with the following primary antibodies: rabbit anti-human/mouse ABCA1 (1:1000; Cell Signaling, 96292), rabbit anti-mouse ApoE (1:1000; Cell Signaling, 49285), mouse anti-human/mouse IL-1 β (1:1000; Cell Signaling, 12242), rabbit anti-mouse iNOS (1:1000; Cell Signaling, 13120), rabbit anti-human/mouse CD206 (1:1000; Cell Signaling, 24595), rabbit anti-human/mouse Arginase 1 (1:1000; Cell Signaling, 93668) and rabbit anti-mouse β -Actin (1:1000; Cell Signaling, 24595). The following day, membranes were washed with 0.1% \times tris-buffered saline with Tween 20, incubated with the goat anti-rabbit or goat anti-mouse horseradish peroxidase-linked secondary antibody (1:20000; Thermo Fisher, 31460 or 31430); then developed using the SuperSignal West Femto Maximum Sensitivity Substrate (ThermoFisher), and imaged with the ChemiDoc Touch Imaging System (Bio-Rad).

Mosue brain histology

Eriochrome cyanine and neutral red (EC) staining were used to visualise lesions for histology in CX3CR1^{CreER}; Rosa26^{idTR} strain. Briefly, brain cryosections were air dried then treated successively with CitriSolv (Fisher Scientific), isopropanol, and 100%, 95%, 90%, 70% and 50% ethanol, for 1 min each. Samples were then washed with distilled water for 1 min, followed by incubation with EC staining solution containing 10% FeCl₃ for 15 min, followed by washing with distilled water for 1 min, then immediately washed with 0.5% NH₄OH for 10 s, followed by another 1 min of washing with distilled water. Samples were then incubated with 1% neutral red solution for 2 min, and washed again with distilled water for 1 min. Finally, samples were dehydrated with successive 1 min washes of 50%, 70%, 90%, 95% and 100% ethanol, 2 min wash of isopropanol, 4 min of CitriSolv, and coverslips were mounted with Acrytol mounting medium (Electron Microscopy Science). Brightfield images were then acquired using \times 20/0.75 NA air objective using the Olympus vs120 Slidescanner. ROIs for lesions were drawn based on lower EC staining surrounded by higher neutral red staining in the region of basal ganglia, and the total areas were analysed using CellSens (Olympus).

Behavioural tests

Locomotor functions were tested before and 1, 3, 7, 14 days after the surgical procedure using rotarod and grip strength. Mice were brought to the testing room 30 min in advance to accommodate before each session. These are details of the methods:

Rotarod

Motor coordination and balance were assessed using a rotarod test. Each mouse was placed on top of the already revolving cylinder (4rpm) facing away from the experimenter, in the orientation opposite to that of the rod movement so that forward locomotion was necessary to avoid a fall. The mice were then exposed to three test trials in which the rotation accelerated from 4 to 30rpm for 5 min. Latency to fall was measured automatically and was averaged over the three trials, with increased latency indicating greater motor coordination and balance. A 3-day training session using a steady rotation speed was conducted before each experiment to diminish the learning effects.

Grip strength

This task measures the forelimb strength. The mouse was allowed to grasp onto a bar with their forelimbs and then gently pulled away by the experimenter. The force at the point when the mouse lost grip was automatically recorded. The test was repeated three times and averaged for each session.

MRI

MRI data were acquired using a 9.4T Bruker BioSpec equipped with a Bruker cryoprobe and operated with ParaVision V.5.1. Mice were anaesthetised initially with 2%–3% isoflurane and a tail vein cannulation was made before imaging. Mice were then head-fixed in an animal carrier using tooth and ear bars. Anaesthesia was maintained by 1.5% isoflurane. Respiration, and body temperature, were non-invasively monitored using a small animal monitoring system (Small Animal Instruments). Initially, a shimming procedure was conducted to correct the distortions and optimise the magnetic field homogeneity follow by a scout scan using FLASH sequence to determine the lesion epicentre and scan range. Subsequently, a high-resolution, T2-weighted sequence (T2WI) was acquired with 16 slices and 0.5 mm thickness using the following parameters: repetition time=4000 ms, echo time=48 ms, acquisition time=512s, flip angle=180°, averages=2, FOV=19.2 \times 19.2 mm², resolution=256 \times 256. Diffusion tensor imaging (DTI) at the same location was implemented using a DtEpi SpinEcho sequence and the following parameters: repetition time=4000 ms, echo time=19.5 ms, spin echo time=0.3584 ms, acquisition time=1120s, flip angle=90°, averages=2, FOV=19.2 \times 19.2 mm², matrix=256 \times 256, segments=4, B0 images=5, gradient directions=30, gradient duration=3.8 ms, diffusion time=8 ms, and b value=2104.8 s/mm². The dynamic contrast-enhanced MRI (DCE-MRI) was then

performed using 3D gradient-echo with flow compensation T1-weighted imaging by using the following parameters: repetition time=20 ms, echo time=3.2 ms, acquisition time=245 s, flip angle=15°, averages=1, FOV=19.2×19.2×1.6 mm³, matrix=192×192×64. One image series was captured as baseline control before the injection of gadopentetate dimeglumine (0.4 mmol/kg, Bayer), followed by five consecutive scans starting immediately after contrast agent was delivered through the catheter.

Lesion volume, haematoma volume and ventricle volume were calculated by the product of slice (0.5 mm) thickness and manually drawn ROI at different slices of T2WI in ImageJ. The hypointense rim on T2WI was selected as lesion, while the hyperintensity within the rim was assigned as haematoma.^{41 42} Parameters of DCE-MRI were generated by algorithms in Jim9 (Xinapse Systems) according to modified Tofts model^{43 44}: $C_t(t) = K_{trans} \int_0^t C_p(\tau) \exp(-K_{trans}(\tau - t) / v_e) d\tau + C_p(t)v_p$. The diffusion data were quantified using restricted diffusion imaging and reconstructed using generalised q-sampling imaging (GQI)^{45 46} in DSI studio with a diffusion sampling length ratio of 0.6. The region of right basal ganglia was manually drawn as ROI and the DTI parameters in ROI were exported. Fibre tracking was based on quantitative anisotropy (QA) and tractography was generated by fibres passing the ROI.

Statistical analyses

Data were collated using Microsoft Excel. Graph generation and statistical hypothesis testing were conducted using GraphPad Prism V.9. Data shown are the individual data point and mean±SD, whereby each point on a bar graph represents a biological replicate. No statistical methods were used to predetermine sample sizes, but our sample sizes were similar to those reported in previous publications.^{47 48} Two mice, each from GW3965 or DMSO group were excluded for all experiments and data collection due to absence of anticipated behavioural deterioration after experimental ICH. Animals were randomised when assigned to various experimental groups and conditions. Data collection and analysis of C57BL/6 wildtype mice were not performed blind to the conditions of the experiment, but all image and data analysis were completed with the same acquisition conditions and analysis thresholds. Tissue sections from CX3CR1^{CreER}; Rosa26^{idTR} strain were blinded for microscopy and analyses. Normal distribution of data was tested using the D'Agostino-Pearson (n≥8) or Shapiro-Wilk (n<8) normality test to verify whether statistical tests were appropriate. The non-parametric Mann-Whitney U test was employed when data did not pass the normality test. Two-way analysis of variance with Bonferroni's multiple comparison's test was used to analyse statistically significant differences among the means of multiple groups with two categorical variables. For all other data that passed the normality test, significance was determined by two-tailed, unpaired t-test or two-tailed, unpaired t-test with Welch's correction when the homogeneity of variance is not fulfilled.

Asterisks indicate significance where *p<0.05, **p<0.01, ***p<0.001, ****p<0.0001.

RESULTS

The LXR agonist GW3965 reduces post-ICH brain injury

To evaluate whether the synthetic LXR agonist GW3965 has overall therapeutic effects when administered after ICH, T2WI was applied to quantify the total lesion volume, haematoma volume and ventricle enlargement following ICH and whether this was affected by GW3965 treatment (figure 1A). The total lesion volume characterised by T2-hypointense rim was reduced in GW3965-treated mice at days 7 and 14 (figure 1B). The haematoma volume represented by T2-hyperintensity at day 7 was decreased by treatment (figure 1C), while the haematoma to lesion ratio was also lower in treated group (figure 1D), suggesting enhanced haematoma clearance. On day 14, measurement of ventricular enlargement as an indicator of brain tissue loss shows that this was lowered by GW3965 (figure 1E), indicating alleviated tissue loss and/or better regeneration by the LXR agonist treatment.

DCE-MRI was applied 7 days after injury to test the permeability of blood-brain barrier (BBB) (figure 1F). There was a tendency of reduced K_{trans} in treatment group (figure 1G), suggesting potentially ameliorated BBB breakdown by GW3965, but no statistical significance was found. There was no difference about V_p between two groups, indicating that blood flow did not contribute to the potential difference of K_{trans} (figure 1H). Collectively, results from MRI suggest GW3965 has favourable effects on collagenase induced preclinical ICH, which prompted us to explore potential mechanisms.

GW3965 elevates LXR downstream gene expression

To address mechanisms by which GW3965 alleviates brain injury following ICH, we determined LXR regulated pathways (ABCA1 and ApoE expression) by tile scans of the whole lesion area of day 7 brain sections using confocal immunofluorescence microscopy (figure 2). While sham mice had barely detectable ABCA1 signal using identical confocal settings (online supplemental figure S1A), the expression of ABCA1 was elevated after ICH in the whole lesion area (figure 2A). Some of the ABCA1 profiles overlapped with Iba1⁺ M/M and minimally with GFAP⁺ astrocytes. The 3D reconstruction and confocal images at perihematoma region exhibited close spatial association between ABCA1 and Iba1⁺ cells (figure 2B,C). The ABCA1 expression was then quantified (see Methods): total ABCA1 expression, the proportion of ABCA1⁺Iba1⁺ and ABCA1⁺GFAP⁺ area were increased by GW3965 compared with DMSO control (figure 2D-F).

Similarly, ApoE was increased mainly at the outer layer of the perihematoma area where it primarily overlapped with GFAP⁺ astrocytes (figure 2G, online supplemental figure S1B). The 3D reconstruction and confocal images at perihematoma region exhibited close spatial association between ApoE and GFAP⁺ cells (figure 2H,I).

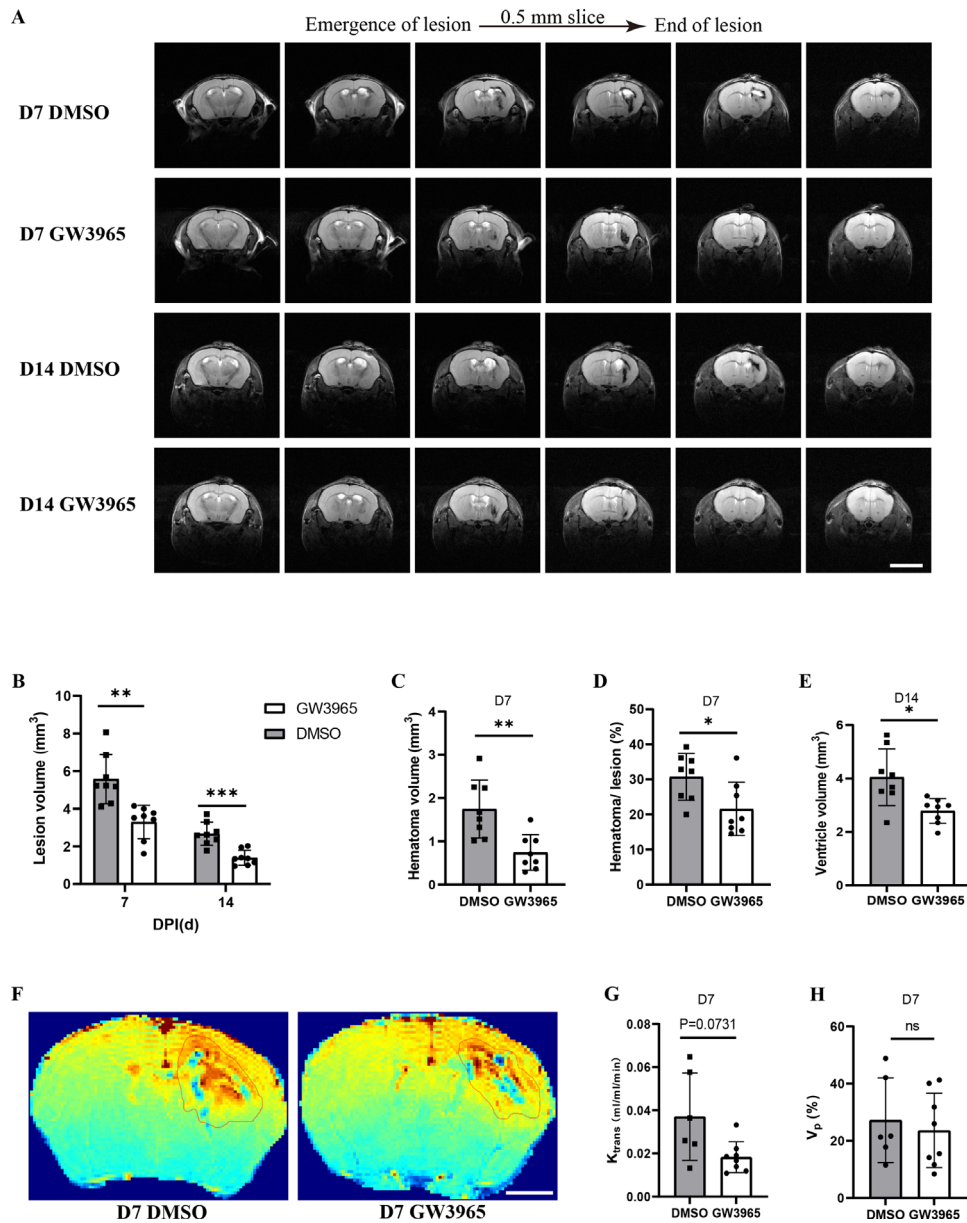


Figure 1 GW3965 accelerates haematoma clearance and alleviates brain tissue loss (A), Representative serial images of T2WI from DMSO-treated and GW3965-treated mice 7 or 14 days after collagenase induced ICH. Scale bar, 5 mm. (B–E), Bar graphs comparing data from T2WI between treatment and control groups: total lesion volume at days 7 and day 14 (B), haematoma volume and haematoma to lesion ratio at day 7 (C, D) and ipsilateral ventricle volume (E); the sample size was $n=8$ per group per time point. (F). Representative images of DCE-MRI from DMSO-treated and GW3965-treated mice 7 days after injury. Scale bar, 2 mm. (G, H), Bar graphs comparing the constant K_{trans} (G) and V_p (H) between two groups at day 7 to evaluate the permeability of blood–brain barrier; the sample size was $n=8$ in GW3965 group but $n=6$ in DMSO group due to failed parameter generation by algorithm from raw data for two mice. DPI, days postinjury; ns, not significant. Significance is indicated as * $p<0.05$, ** $p<0.01$, *** $p<0.001$; two-tailed, unpaired t-test (B–D, H) or two-tailed, unpaired t-test with Welch’s correction (E, G). Bar graphs show individual data points and represent mean \pm SD. DCE, dynamic contrast-enhanced; DPI, days postinjury; ICH, intracerebral haemorrhage; NS, not significant; T2WI, T2-weighted image.

Quantification showed upregulated ApoE expression and the increased ratio of ApoE⁺GFAP⁺ area in GW3965 treatment group (figure 2J,K). In contrast, the fractional ApoE⁺Iba1⁺ area was not significant between groups (figure 2L). Overall, the elevated ABCA1 in phagocytes may promote cholesterol and lipid efflux and recycling, while the increased ApoE would provide increased carrier capacity for lipid transport.

We also evaluated the expression of ABCA1 and ApoE at perimhaematoma regions using real-time qPCR (online supplemental figure S2A,B) and western blot (online supplemental figure S2C–E). Quantification showed that the transcripts and protein content of these genes were elevated after 7-day GW3965 treatment (online supplemental figure S2A–E), which is similar to the results from confocal data.

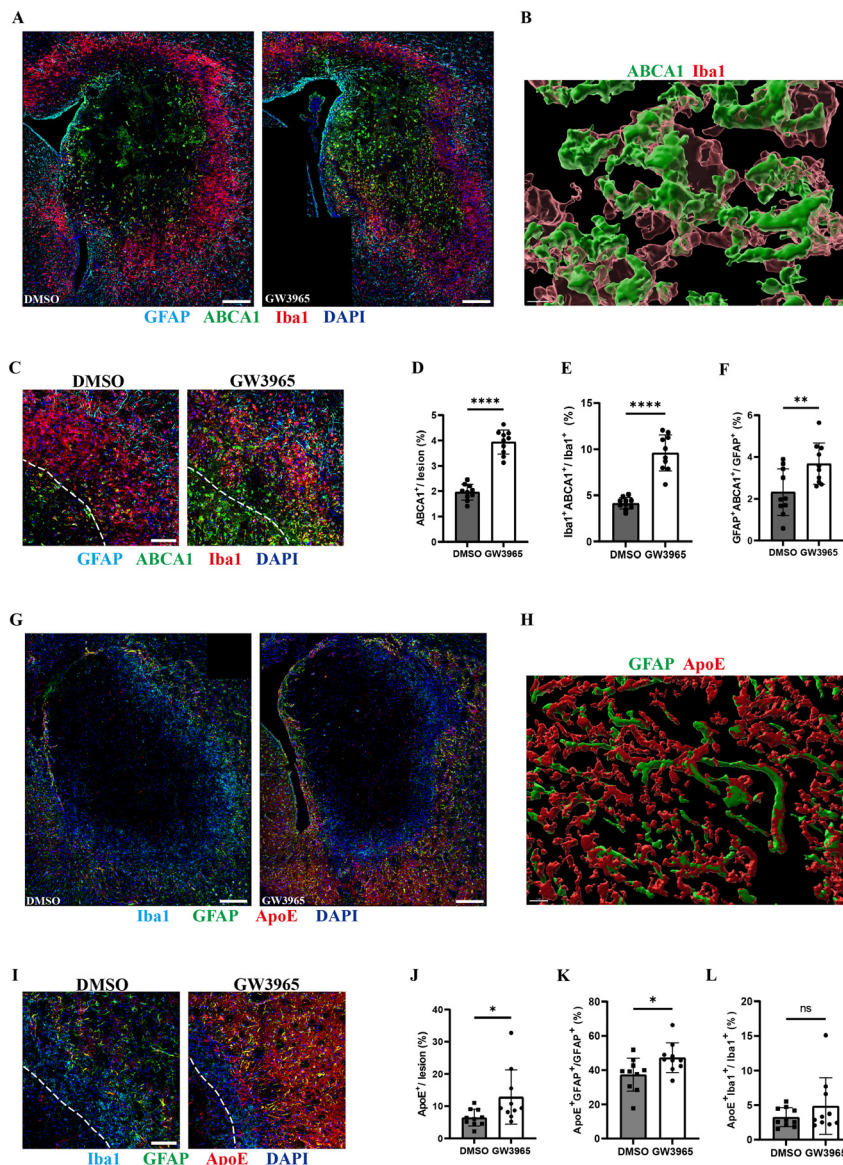


Figure 2 GW3965 upregulates LXR downstream-gene expression. (A) Representative images of confocal tile scan showing whole day 7 lesion labelled with DAPI (blue), GFAP (Cyan), ABCA1 (green) and Iba1 (red). Scale bar, 200 μ m. (B) Representative image of a three-dimensional (3D) reconstruction of a perihæmatomal region in the treatment group using Imaris. Scale bar, 3 μ m. (C) Representative confocal images of perihæmatomal region labelled with DAPI (blue), GFAP (cyan), ABCA1 (green) and Iba1 (red). The left corner within dotted lines depicts lesion centre. Scale bar, 100 μ m. (D–F), Bar graphs comparing the ABCA1⁺ percentage (D), Iba1⁺ABCA1⁺ over Iba1⁺ proportions (E) and GFAP⁺ABCA1⁺ over GFAP⁺ proportions (F) between GW3965 treatment and DMSO control within the lesion region at day 7; the sample size was n=10 per group. (G) Representative images of confocal tile scan showing whole day 7 lesion labelled with DAPI (blue), Iba1 (cyan), GFAP (green) and ApoE (red). Scale bar, 200 μ m. Scale bars are not equal. (H), Representative image of a 3D reconstruction of a perihæmatomal region in the treatment group using Imaris. Scale bar, 7 μ m. (I), Representative confocal images of perihæmatomal region labelled with DAPI (blue), Iba1 (cyan), GFAP (green) and ApoE (red). The left corner within dotted lines is the lesion centre. Scale bar, 100 μ m. (J–L), Bar graphs comparing the ApoE⁺ percentage (J), GFAP⁺ApoE⁺ over GFAP⁺ proportions (K) and Iba1⁺ApoE⁺ over Iba1⁺ proportions (L) between GW3965 treatment and DMSO control within the lesion region at day 7; the sample size was n=10 per group. Significance is indicated as *p<0.05, **p<0.01, ****p<0.0001; two-tailed, unpaired t-test (D, F, K); or two-tailed, unpaired t-test with Welch's correction (E); or Mann-Whitney U test (J, L). Bar graphs show individual data points and represent mean \pm SD. ApoE, apolipoprotein E; LXR, liver X receptor.

LXR agonist appears to promote phenotype change of M/M

We evaluated IL1 β expression as it is a target gene of LXR trans-repression.^{31 33} IL1 β was distributed predominantly in the same area as Iba1 positive M/M at the perihæmatomal region (figure 3A–C). Iba1 and IL1 β

expression was downregulated by GW3965 in the lesion area (figure 3D,E), and the proportion of Iba1⁺IL1 β ⁺ M/M was also reduced (figure 3F).

With the reduced IL1 β ⁺ M/M, and as IL1 β ⁺ is an indicator of the proinflammatory nature of myeloid cells, we evaluated

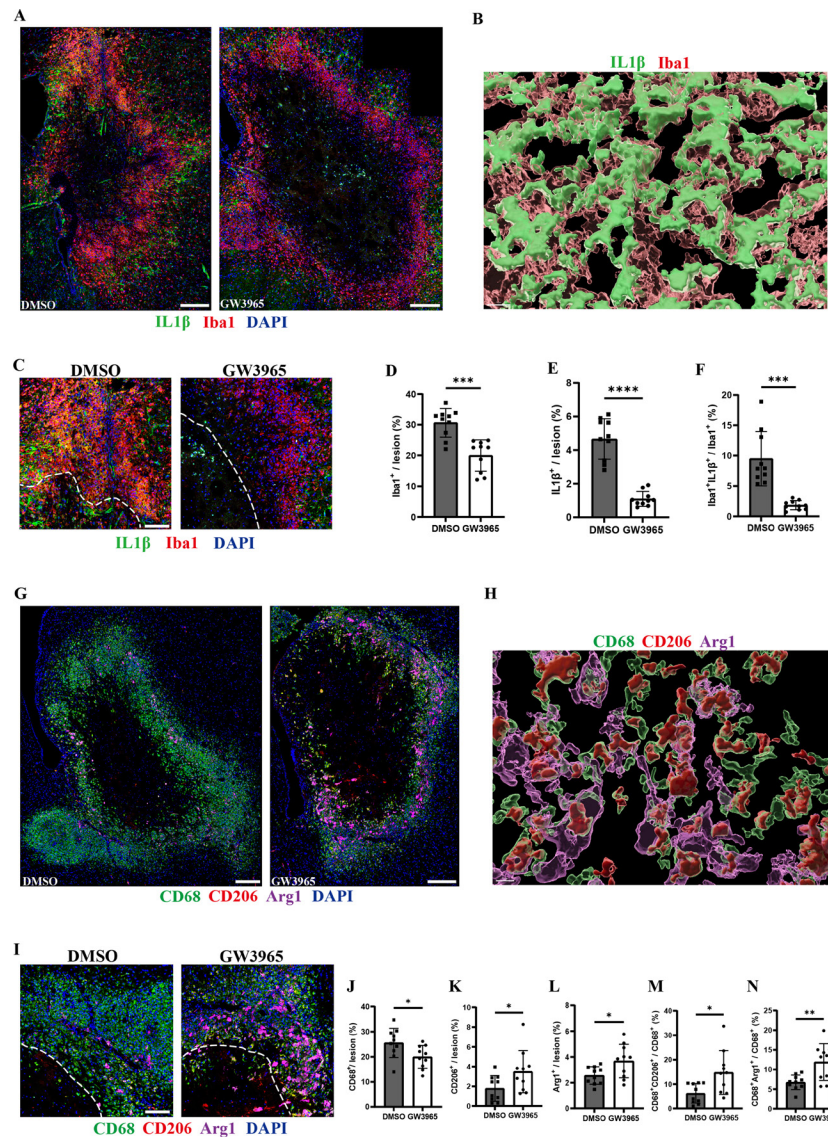


Figure 3 Enhanced LXR activation promotes M/M phenotype shifting. (A) Representative images of confocal tile scan showing whole day 7 lesion labelled with DAPI (blue), IL1 β (green) and Iba1 (red). Scale bar, 200 μ m. The size of images (note the longer scale bar in the GW3965 group) is adjusted to present the whole lesion within each frame. (B) Representative image of a three-dimensional (3D) reconstruction of a perihematoma region in the vehicle group using Imaris. Scale bar, 5 μ m. (C) Representative confocal images of perihematoma region labelled with DAPI (blue), IL1 β (green) and Iba1 (red), the left corner within dot lines orients the lesion centre. Scale bar, 100 μ m. (D–F) Bar graphs comparing the Iba1⁺ percentage (D) IL1 β ⁺ percentage (E) Iba1⁺IL1 β ⁺ over Iba1⁺ proportions (F) between GW3965 treatment and DMSO control within the lesion region at day 7; the sample size was n=10 per group. (G) Representative images of confocal tile scan showing whole day 7 lesion labelled with DAPI (blue), CD68 (green), CD206 (red) and Arg1 (magenta). Scale bar, 200 μ m. Scale bars are not equal. (H) Representative image of a 3D reconstruction of a perihematoma region in the treatment group using Imaris. Scale bar, 10 μ m. (I) Representative confocal images of perihematoma region labelled with DAPI (blue), CD68 (green), CD206 (red) and Arg1 (magenta); the left corner within dotted lines denotes the lesion centre. Scale bar, 100 μ m. (J–N) Bar graphs comparing the CD68⁺ percentage (J), CD206⁺ percentage (K), Arg1⁺ percentage (L) CD68⁺CD206⁺ over CD68⁺ proportions (M) and CD68⁺Arg1⁺ over CD68⁺ proportions (N) between GW3965 treatment and DMSO control within the lesion region at day 7; the sample size was n=10 per group. Significance is indicated as *p<0.05, **p<0.01, ***p<0.001, ****p<0.0001; two-tailed, unpaired t-test (D, J–L) or two-tailed, unpaired t-test with Welch's correction (E, F, M, N). Bar graphs show individual data points and represent mean \pm SD. LXR, liver X receptor; M/M, microglia/macrophage.

if GW3965 affected Arg1 and CD206, which are often used as regulatory markers of myeloid cells.^{5 49} Figure 4G–I displays representative staining in tissue from GW3965 or DMSO-treated animals. Consistent with lowered Iba1 percentage, CD68⁺ area was reduced in GW3965 compared

with DMSO control sections (figure 3J). Conversely, the expression of regulatory markers in the lesion was upregulated (figure 3K,L), and the fraction of CD68⁺Arg1⁺ and CD68⁺CD206⁺ in total M/M was increased after 7-day GW3965 treatment (figure 3M,N).

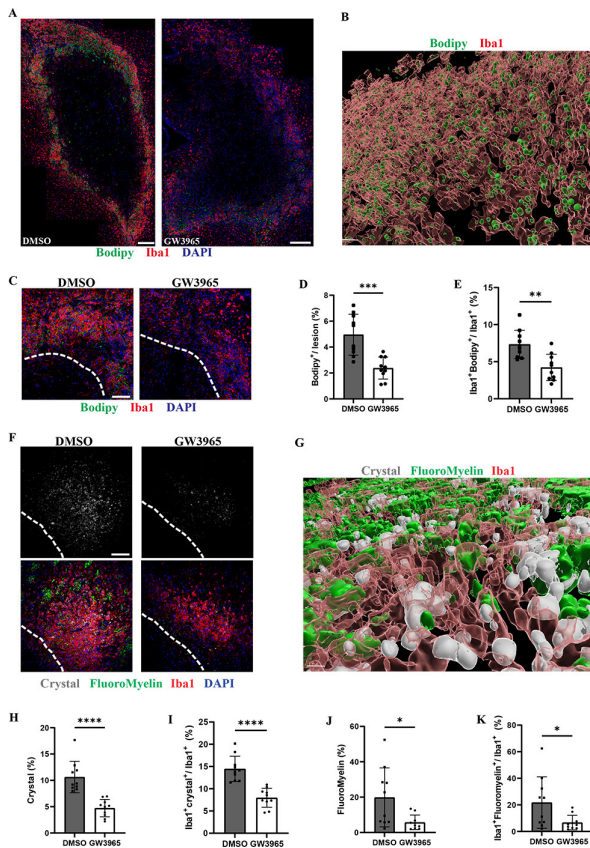


Figure 4 Enhanced LXR activation mitigates lipid accumulation in phagocytes. (A) Representative images of confocal tile scan showing whole day 7 lesion labelled with DAPI (blue), Bodipy (green) and Iba1 (red). Scale bar, 200 μ m. The size of images images (note the longer scale bar in the GW3965 group) is adjusted to present the whole lesion within each frame. (B) Representative image of a three-dimensional (3D) reconstruction of a day 7 perihematoma region in the vehicle group using Imaris, showing Iba1⁺ phagocytes enveloping Bodipy⁺ material. Scale bar, 15 μ m. (C) Representative confocal images of perihematoma region labelled with DAPI (blue), Bodipy (green) and Iba1 (red); the left corner within dotted lines depicts the lesion centre. Scale bar, 100 μ m. (D, E), Bar graphs comparing the Bodipy⁺ percentage (D) and Iba1⁺Bodipy⁺ over Iba1⁺ proportions (E) between GW3965 treatment and DMSO control within the lesion region at day 7; the sample size was n=10 per group. (F) Representative confocal images of day 7 perihematoma region labelled with DAPI (blue), crystal (grey), Fluoromyelin (green) and Iba1 (red); the left corner within dotted lines is the lesion centre. Scale bar, 100 μ m. (G) Representative image of a 3D reconstruction of a day 7 perihematoma region in the vehicle group using Imaris, showing Iba1⁺ phagocytes enveloping crystal and Fluoromyelin⁺ material. Scale bar, 10 μ m. (H–K) Bar graphs comparing the crystal⁺ percentage (H) Iba1⁺crystal⁺ over Iba1⁺ proportions (I) Fluoromyelin⁺ percentage (J) and Iba1⁺Fluoromyelin⁺ over Iba1⁺ proportions (K) between GW3965 treatment and DMSO control within the perihematoma region at day 7; the sample size was n=10 per group. Significance is indicated as *p<0.05, **p<0.01, ***p<0.001, ****p<0.0001; two-tailed, unpaired t-test (D, E, H, I) or two-tailed, unpaired t-test with Welch’s correction (J, K). Bar graphs show individual data points and represent mean \pm SD. LXR, liver X receptor.

To corroborate the results from confocal microscopy, western blot was used to evaluate the expression of M/M markers in day 7 perihematoma regions (online supplemental figure S2F). The expression of proinflammatory IL-1 β and iNOS was inhibited by GW3965 treatment (online supplemental figure S2G,H), while that of regulatory/repair markers including CD206 and Arg1 was upregulated (online supplemental figure S2I,J).

LXR agonist alleviates lipid burden of phagocytes

To corroborate that GW3965 promoted lipid/cholesterol efflux from ICH lesions as indicated by elevation of ABCA1 and ApoE, we quantified neutral-lipid droplets within M/M using Bodipy staining in day 7 samples. Interestingly, Bodipy⁺ droplets were distributed in the same area as Iba1⁺ cells at perihematoma region at day 7 (figure 4A–C) and throughout the lesion at day 14 (online supplemental figure S3A), which may indicate that myelin and cellular debris were gradually phagocytosed by myeloid cells from the outer to the inner region. A 3D reconstruction of perihematoma region showed much of the Bodipy stains were inside Iba1⁺ cells instead of just overlapping them (figure 4B), suggesting existence of lipid-laden M/M and ongoing phagocytosis. Total Bodipy accumulation in the whole lesion and the fraction of lipid-laden phagocytes were alleviated by GW3965 on day 7 (figure 4D,E) and day 14 (online supplemental figure S3B,C) compared with the vehicle.

The formation of cholesterol crystals inside phagocytes is reported to destabilise lysosomes and to lead to more proinflammatory features.^{39 50} As a myelin-rich brain region in mice, the striatum after haemorrhage would be exposed to a large amount of cholesterol from degenerating myelin, which could be processed by M/M. The Bodipy stain recognises all neutral lipids including cholesterol ester, so we next evaluated specifically the accumulation of cholesterol crystals within phagocytes. By combining laser reflection,^{30 38 39} and FluoroMyelin (which stains intact and degraded myelin) and Iba1 staining, we found crystal-loaded and myelin debris-loaded phagocytes in the perihematoma area of day 7 samples (figure 4F). IMARIS reconstruction documented myelin debris and crystals within Iba1⁺ phagocytes (figure 4G). In the perihematoma area of day seven lesions, less crystal, degraded myelin, and crystal/myelin debris-laden phagocytes were observed in GW3965 treated mice (figure 4H–K).

LXR agonist promotes oligodendrogenesis and reduces white matter injury

Deficient cholesterol efflux from phagocytes has been reported to hinder remyelination due to exacerbated inflammation and insufficient cholesterol recycling.^{29 30} As GW3965 elevated expression of ABCA1, ApoE and enhanced lipid/cholesterol clearance, we addressed whether this may contribute to oligodendrogenesis, remyelination and axonal protection. We evaluated Olig2⁺ oligodendrocyte lineage cells at the perihematoma area

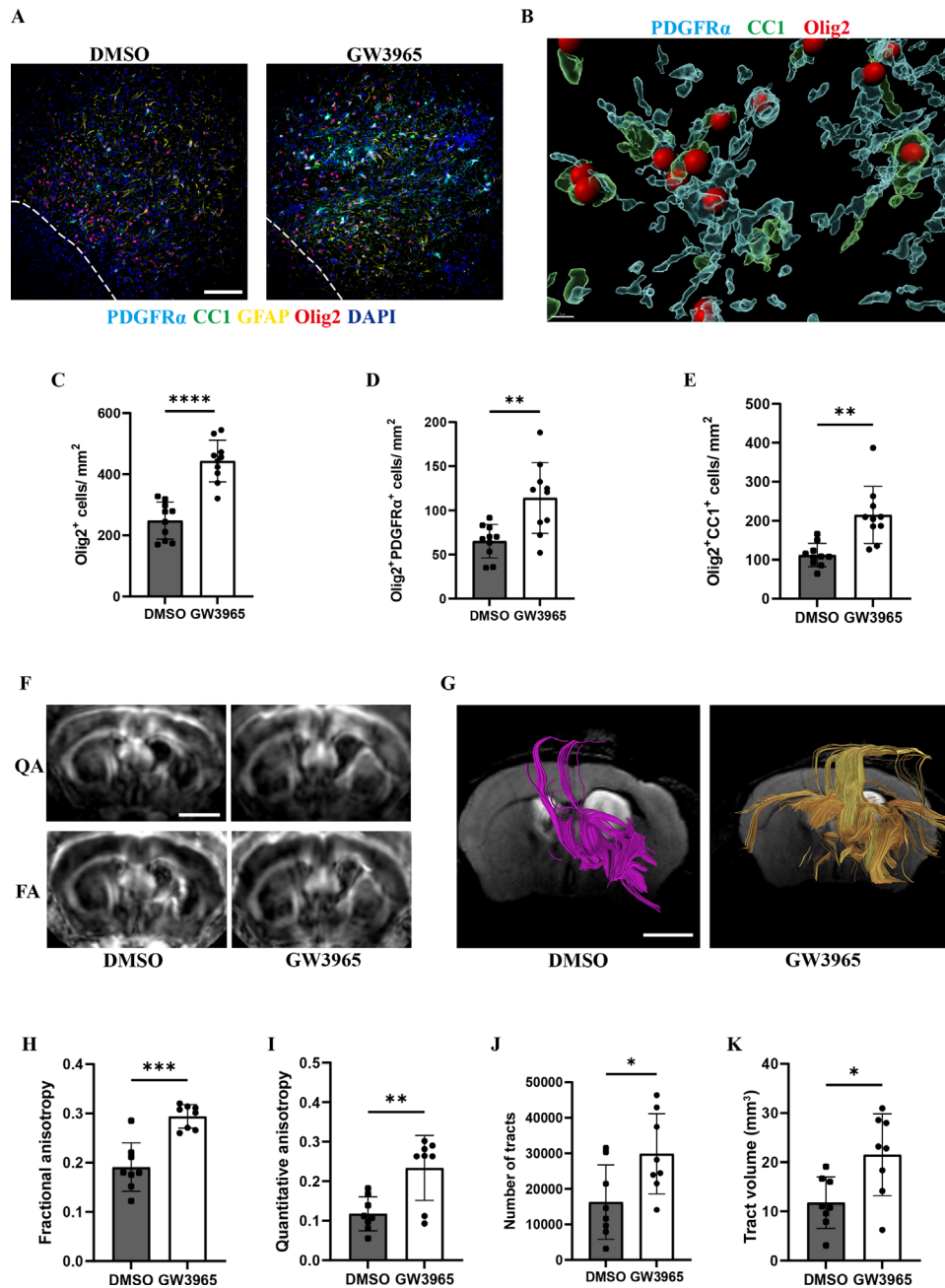


Figure 5 Enhanced LXR signalling boosts oligodendrogenesis and reduces white matter injury. (A) Representative confocal images of day 7 perihematoma regions labelled with DAPI (blue), PDGFR α (cyan), CC1 (green), GFAP (yellow) and Olig2 (red); the left corner within dotted lines orients the lesion centre. Scale bar, 100 μ m. (B) Representative image of a three-dimensional reconstruction of a day 7 perihematoma region in the treatment group using Imaris. (C–E) Bar graphs comparing the density of Olig2 $^{+}$ cells (C) Olig2 $^{+}$ PDGFR α $^{+}$ cells (D) and Olig2 $^{+}$ CC1 $^{+}$ cells (E) between GW3965 treatment and DMSO control within the perihematoma region at day 7; the sample size was n=10 per group. (F) Representative DTI images generated by quantitative anisotropy (QA) or fractional anisotropy (FA) at day 14. Scale bar, 2 mm. (G) Representative images of tractography. Scale bar, 2 mm. (H–K) Bar graphs comparing the fractional anisotropy (H) quantitative anisotropy (I) number of tracts (J) or total volume of tracts (K) between GW3965 treatment and DMSO control within or through the region of basal ganglia at day 14; the sample size was n=8 per group. Significance is indicated as * p <0.05, ** p <0.01, *** p <0.001, **** p <0.0001; two-tailed, unpaired t-test (C, H–K) or two-tailed, unpaired t-test with Welch’s correction (D–E). Bar graphs show individual data points and represent mean \pm SD. DTI, diffusion tensor imaging; LXR, liver X receptor.

of day 7 tissue sections, as these cells were found gathered in this location (figure 5A). GFAP $^{+}$ astrocytes were used to navigate the field selection when imaging. The numbers of Olig2 $^{+}$, Olig2 $^{+}$ PDGFR α $^{+}$ (representing oligodendrocyte

precursor cells) and Olig2 $^{+}$ CC1 $^{+}$ cells (mature oligodendrocytes) were all increased by GW3965 treatment (figure 5C–E). We were unsuccessful at evaluating remyelination in part because we could not differentiate

degenerating myelin from intact ones (online supplemental figure S4).

Importantly, the DTI sequence and tractography on MRI provided insights on axonal injury (figure 5F,G). Compared with DMSO control, both fractional anisotropy (FA) and QA were higher in the striatum of GW3965 treated mice at day 14 (figure 5H,I), indicating alleviated injury of white matter bundles in that region. Tractography was conducted based on QA due to its better specificity and sensitivity,^{51 52} and more tracked fibres were documented in the treatment group (figure 5J,K).

GW3965 promotes NSC expansion and functional recovery

To evaluate whether GW3965 affected the proliferation and survival of NSCs, SOX2, nestin and Ki67 stains were conducted on day 14 lesion (figure 6A,B) and in the subventricular zone (SVZ) (figure 6C,D). SOX2⁺, SOX2⁺Ki67⁺ cells and nestin⁺ area were increased in the lesion (figure 6E–G) and SVZ (figure 6H–J) by GW3965 treatment, suggesting enhanced expansion of NSCs.

Rotarod and grip strength tests were used to evaluate if the GW3965 treatment alleviated neurological deficits and promoted functional recovery after experimental ICH. To exclude the possibility that GW3965 might enhance physical performance or have adverse neurological effects during normal conditions, both sham and ICH groups received either GW3965 or the DMSO vehicle. Both rotarod and grip strength data showed no significant difference at each time point between DMSO and GW3965 treated sham groups, suggesting no adverse toxicity of GW3965, and there was no behavioural change over the course of the experiment compared with baseline (figure 6K,L). In ICH mice, the performance of both DMSO and GW3965 groups dropped from the day after haemorrhage. Thereafter (day 3), GW3965 treatment improved the latency before falling in the rotarod test, and enhanced forelimb strength compared with DMSO control; this therapeutic difference was maintained through 14 days (figure 6M,N). Indeed, GW3965 treated mice showed no significant difference at day 14 after ICH compared with baseline in the rotarod test (figure 6M).

The therapeutic effects of GW3965 are abrogated in mice deficient of M/M

To evaluate if M/M are indispensable for GW3965 mediated beneficial effects in experimental ICH, we tested locomotor function, brain injury and tissue regeneration after conditional depletion of M/M using CX3CR1^{CreER};Rosa26^{idTR} mice. DT-injected mice with M/M depletion (see figure 7D) showed no significant difference between GW3965 treatment and DMSO control group in rotarod test at each time point examined (online supplemental figure S8A). In contrast, GW3965 appeared to improve functional performance 7 days after ICH in mice that did not receive DT; the p value of 0.0726 is likely due to the small sample size and the high individual variance in behavioural scores (online supplemental figure S8A). The reduction of total lesion volume by GW3965 after

ICH was reproduced in M/M intact mice but not when M/M were depleted (figure 7B,C). Mice that received DT showed larger lesion volume in general compared with non-M/M-depleted controls (figure 7B,C). The Iba1⁺ M/M were significantly reduced after DT-induced depletion (figure 7D,E). The number of Olig2⁺ oligodendrocyte lineage cells was higher in GW3965 treated non-M/M-depleted group compared with DMSO control at day 7 perihematoma regions (figure 7D,F); this difference was lost in M/M-depleted mice (figure 7D,F). SOX2⁺ cells, nestin⁺ area SOX2⁺DCX⁺ cells were increased in the SVZ of M/M intact mice by GW3965 treatment (figure 7G–I), but this no longer manifest after DT-induced M/M depletion (figure 7G–I; online supplemental figure S8B). Collectively, M/M appear crucial to the therapeutic effects of LXR after ICH.

DISCUSSION

Secondary brain injury and limited tissue repair after ICH are associated with poor prognosis, and the functions and phenotypes of M/M are a key determinant of these two processes.^{3–5} The evolution of striatal lesions and functional deficits in mice were documented at different time points following collagenase-induced ICH. CD68⁺ M/M were elevated at the perihematoma region, peaked at day 7 and proceeded to encompass the entire lesion centre correspondent with resorption of haematoma evident through reduction of lesion size. GFAP⁺ astrocytes were aggregated at the outer layer of perihematoma region and NeuN⁺ neurons were not evident in the lesion. Olig2⁺ oligodendrocyte lineage cells aggregated at the edge of lesion accompanied first by disappearance and subsequently with recurrence of MBP staining in the same area as the haematoma resolved, suggesting a regenerative process. Unlike the progression and apparent recovery of lesion, neurological deficits persisted through 14 days of injury. Because LXR signalling functions in both cholesterol efflux and anti-inflammatory outcomes, we treated ICH mice with GW3965 to determine if this LXR agonist could modulate M/M phenotype and tissue regeneration. By applying MRI and behavioural tests, we found that 7-day GW3965 treatment reduced brain injury, tissue loss and white matter injury, associated with improved functional recovery. Confocal imaging showed that GW3965 facilitated the change of proinflammatory phagocytes into regulatory ones, while the cholesterol crystal and lipid burden were reduced. Moreover, GW3965 promoted oligodendrogenesis in perihematoma regions and enhanced NSC proliferation and density in lesion and SVZ. Despite the promising results, one caveat to be noted is that the data from C57Bl/6J wild-type mice were not performed in a blinded manner, although all image and data analysis were completed with the same acquisition conditions and analysis thresholds.

In a previous study, a synthetic LXR agonist, T0901317, was reported to inhibit proinflammatory molecules including IL-6, iNOS and cyclooxygenase-2 in the early

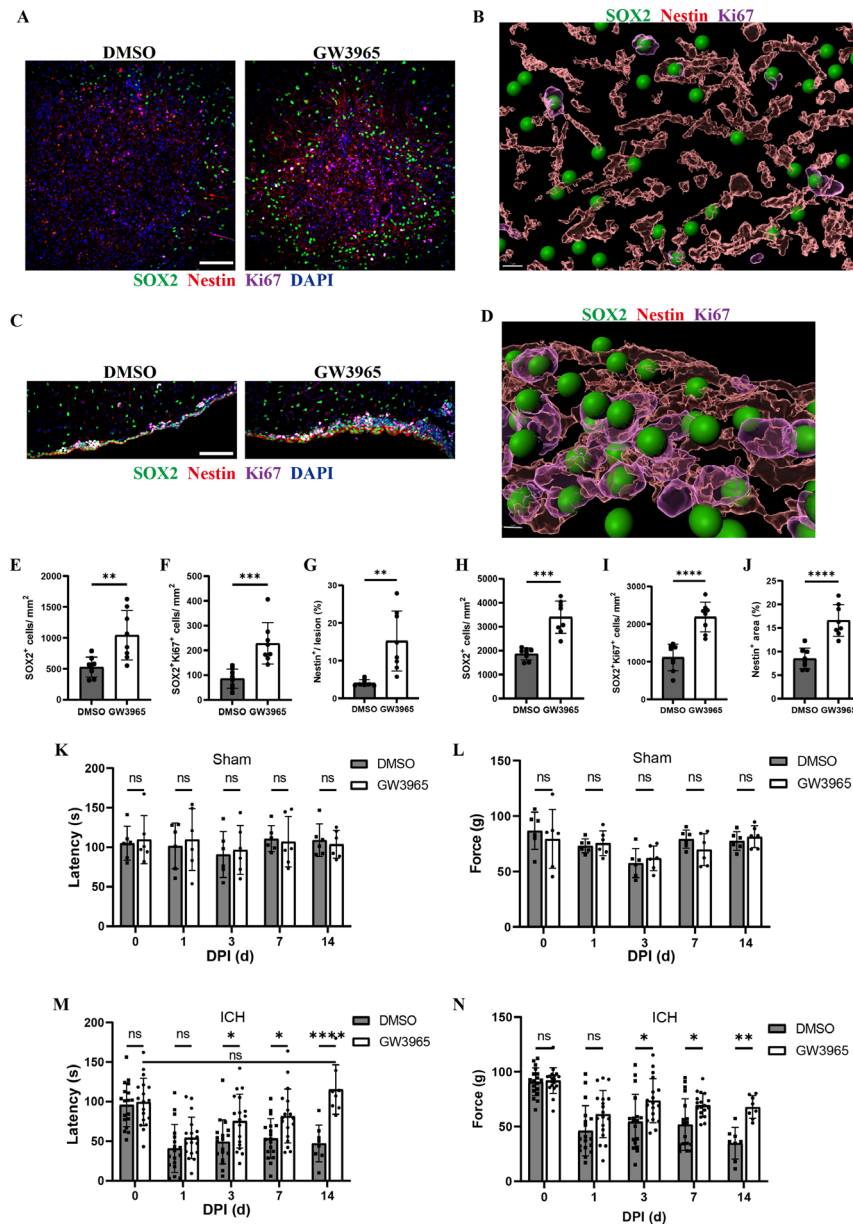


Figure 6 GW3965 treatment promotes NSC proliferation and functional recovery. (A) Representative confocal images of day 14 lesion region labelled with DAPI (blue), SOX2 (green), Nestin (red) and Ki67 (magenta). Scale bar, 100 μ m. (B), Representative image of a three-dimensional (3D) reconstruction within a day 14 lesion in the treatment group using Imaris. (C) Representative confocal images of day 14 subventricular zone (SVZ) labelled with DAPI (blue), SOX2 (green), Nestin (red), and Ki67 (magenta). Scale bar, 100 μ m. (D), Representative image of a 3D reconstruction at day 14 SVZ in the treatment group using Imaris. (E–J), Bar graphs comparing the density of SOX2⁺ cells (E, H), SOX2⁺Ki67⁺ cells (F, I) or Nestin⁺ percentage (G, J) in the lesion (E–G) or SVZ (H–J) between GW3965 treatment and DMSO control at day 14; the sample size was n=8 per group. (K–N), Bar graphs comparing the latency of rotarod (K, M) or forelimb force of grip strength test (L, N) between treatment and vehicle groups in sham (K–L) or ICH (M–N) mice at different time points before and after the injury; the sample size was n=6 per sham group; n=18 per ICH group before and 1, 3, 7 days after the injury, n=8 per ICH group 14 days after injury. Significance is indicated as *p<0.05, **p<0.01, ***p<0.001, ****p<0.0001; two-tailed, unpaired t-test (F, I–J); two-tailed, unpaired t-test with Welch's correction (E, G–H); or two-way ANOVA with Bonferroni's multiple comparison's test (K–N). Bar graphs show individual data points and represent mean \pm SD. ANOVA, analysis of variance; DPI, days postinjury; ICH, intracerebral haemorrhage; ns, not significant; NSC, neural stem cell.

phase after collagenase induced ICH.⁵³ However, the authors did not address whether the enhanced LXR signalling promoted M/M phenotype shifting, cholesterol recycling and tissue regeneration.

Here, we first demonstrate that there appeared to be a phenotype shift of M/M as evident by less IL1 β ⁺Iba1⁺ cells, and more Arg1⁺CD68⁺ and CD206⁺CD68⁺ cells in treated mice, suggesting that the proinflammatory

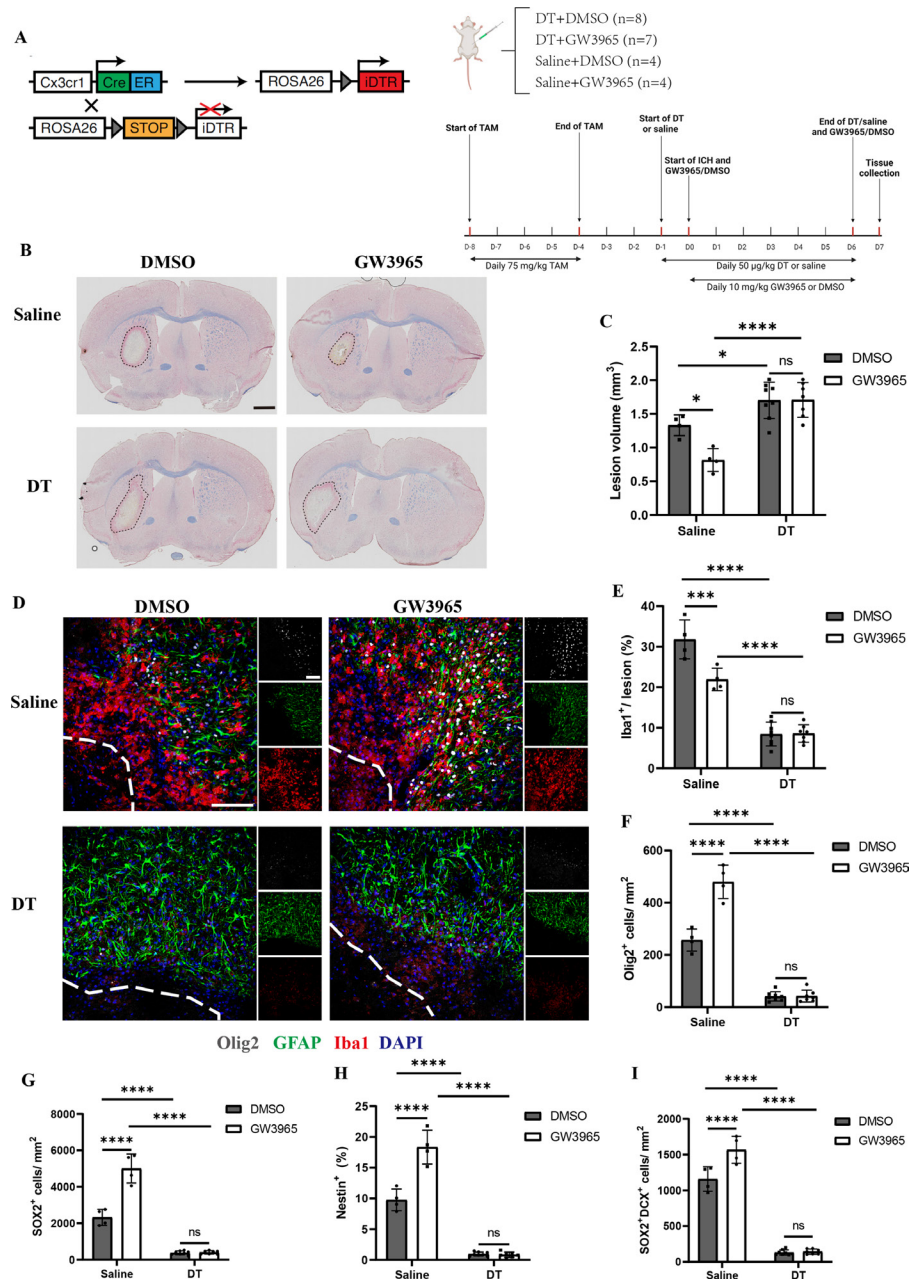


Figure 7 The therapeutic effects of GW3965 appear to involve microglia/macrophages. (A) Schematic of the experimental design. (B) Representative images of EC staining 7 days after injury. Scale bar, 1 mm. (C) Bar graph comparing the day 7 lesion volume calculated from EC staining among groups including saline+DMSO, saline+GW3965, DT+DMSO and DT+GW3965; the sample size was n=4 per saline group; n=8 for DT+DMSO group; n=7 for DT+GW3965 group. (D) Representative confocal images of day 7 perihematoma regions labelled with DAPI (blue), Olig2 (grey), GFAP (green) and Iba1 (red), the left corner within dotted lines denotes the lesion centre. Scale bar, 100 μ m. (E, F) Bar graphs comparing the Iba1⁺ percentage (E) or Olig2⁺ cell density (F) at day 7 perihematoma regions among groups including saline+DMSO, saline+GW3965, DT+DMSO and DT+GW3965; the sample size was n=4 per saline group; n=8 for DT+DMSO group; n=7 for DT+GW3965 group. (G–I) Bar graphs comparing the density of SOX2⁺ cells (G), Nestin⁺ percentage (H) or SOX2⁺DCX⁺ cell density (I) at day 7 SVZ among groups including saline+DMSO, saline+GW3965, DT+DMSO and DT+GW3965; the sample size was n=4 per saline group; n=8 for DT+DMSO group; n=7 for DT+GW3965 group. Significance is indicated as *p<0.05, ***p<0.001, ****p<0.0001; two-way ANOVA with Bonferroni's multiple comparison's test. Bar graphs show individual data points and represent mean \pm SD. ANOVA, analysis of variance; DT, diphtheria toxin; EC, eriochrome cyanine; TAM, tamoxifen.

property of these cells was inhibited while their regulatory properties were promoted. In addition to immunomodulation, the enhanced cholesterol efflux and transport by LXR activation have been shown to facilitate

neurogenesis, axonal regeneration and remyelination in ischaemic or demyelination models,^{28 29 54} while deficient LXR signalling may result in impaired tissue regeneration after CNS injury due to insufficient cholesterol

recycling from phagocytes.^{30–38} We observed alleviated lipid droplets and cholesterol crystal accumulation within phagocytes in association with more Olig2⁺PDGFR α ⁺, Olig2⁺CC1⁺, SOX2⁺ Ki67⁺ and nestin⁺ cells in treated mice; this suggests that boosted activation of LXR signaling aided tissue regeneration by providing recycled cholesterol that the repair process would need. More importantly, we found that the alleviated brain injury and enhanced tissue regeneration were neutralised by M/M conditional depletion using CX3CR1^{CreER}:Rosa26^{iDTR} strain, indicating the modulation of M/M is crucial for beneficial effects of GW3965. However, our analyses of specific molecular mechanisms was superficial due to the limitation of resource and time. Future experiments will include ABCA, ABCG and ApoE conditional knockout strains combined with scRNAseq or CyTOF to investigate the casual relationship between LXR downstream genes and the outcomes after experimental ICH, and to unravel specific mechanisms in various cell clusters.

Given the difficulty of discriminating functional axons from degenerating and destroyed ones, we tried to counterstain neurofilament with an APP antibody to inform on compromised axons. However, APP was elevated in the day 14 lesion and in the SVZ compared with normal tissue, and this did not overlap with axons or myeloid cells. There tended to be more APP⁺ cells in the lesion of GW3965 group, but no statistical significance was found. Due to the association between APP and neurogenesis,^{55–57} we hypothesised that the elevated APP⁺ cells comprised of NSCs and, indeed, there was more APP⁺SOX2⁺ cells in the lesion area of GW3965 mice, suggesting enhanced neurogenesis. Moreover, we found increased SOX2⁺DCX⁺ cells in SVZ of GW3965 treated M/M undepleted CX3CR1^{CreER}:Rosa26^{iDTR} mice, which supports the hypothesis that LXR agonist can promote neurogenesis after experimental ICH.

Cholesterol efflux and immunomodulation are linked since the crystal inside phagocytes can destabilise lysosomes and make cells more proinflammatory⁵⁰; moreover, the lipid overload could impair the phagocytotic ability of M/M so that the remnant debris within lesions could trigger proinflammatory responses.⁵⁸ Our data suggest that the anti-inflammatory outcome of LXR activation along with cholesterol recycling provide a better regenerative microenvironment for oligodendrocytes and NSCs. In addition to histology-verified outcomes, these favourable outcomes after GW3965 treatment were corroborated by T2 and DTI MRI sequences, coincident with recovery of behavioural deficits.

The lipogenesis effects of LXR agonists may potentially cause dyslipidaemia and hepatic steatosis, which limit clinical translation.^{59–61} Moreover, a clinical trial testing another synthetic LXR agonist reported CNS-related neurological or psychiatric adverse events in healthy participants.⁶² Compared with other LXR agonists such as T0901317, GW3965 has more LXR β and less LXR α activity (EC50 of 30 and 190 nM, respectively), which may result in less unfavourable lipogenesis effects that are

mainly mediated by LXR α in rodents.^{63–64} These factors account for our selection of GW3965 in this study. We did not find impaired locomotor function in GW3965-sham group in our study. The short treatment duration (7 days) of GW3965 or other LXR agonists may also obviate significant toxicity if translated to patients after ICH.

In summary, we demonstrate that the LXR agonist GW3965 reduced lesion volume, white matter injury and brain tissue loss, while promoting tissue regeneration in experimental ICH, and these therapeutic effects were associated with M/M. Potential mechanisms may include the phenotype shift and cholesterol efflux of M/M, creating a more permissive environment for oligodendrogenesis and neurogenesis. Even with possible adverse lipogenesis effects, the neuroprotective and regenerative benefits of short-term LXR agonism demonstrated in this study make them promising for use in clinical ICH.

Author affiliations

¹Department of Cerebrovascular Diseases, The Second Affiliated Hospital of Zhengzhou University, Zhengzhou, Henan, China

²Academy of Medical Science, Zhengzhou University, Zhengzhou, Henan, China

³Hotchkiss Brain Institute and Department of Clinical Neurosciences, University of Calgary, Calgary, Alberta, Canada

⁴Department of Biochemistry, Microbiology, & Immunology, College of Medicine, University of Saskatchewan, Saskatoon, Saskatchewan, Canada

⁵Department of Radiology, University of Calgary, Calgary, Alberta, Canada

Contributors RZ conceived the project, designed, performed and analysed experiments, wrote the first draft of the paper and is the guarantor of this study. YD and DM helped with histology and confocal imaging. YL helped with molecular experiments. SG and RM helped with animal administration and the surgical process. BML provided suggestions for image analysis. JFD helped with MRI experiment design and analysis. VWY and MX helped co-conceive the project, provided support and supervised the overall study and critically edited the manuscript. All authors reviewed and edited the manuscript.

Funding The authors acknowledge operating grant support from the Canadian Institutes of Health Research (Foundation grant 1049959) (VWY); and from the National Key Research and Development Program of China (grant no: 2018YFC1312200) and the National Natural Science Foundation of China (grants no: 82071331, 81870942 and 81520108011) (MX). RZ is supported by a PhD studentship from the China Scholarship Council.

Competing interests None declared.

Patient consent for publication Not applicable.

Ethics approval All experiments were conducted with ethics approval from the Animal Care Committee at the University of Calgary under regulations of the Canadian Council of Animal Care, protocol no. AC21-0073.

Provenance and peer review Not commissioned; externally peer reviewed.

Data availability statement Data are available on reasonable request. The data that support the findings of this study are available from the corresponding authors on reasonable request.

Supplemental material This content has been supplied by the author(s). It has not been vetted by BMJ Publishing Group Limited (BMJ) and may not have been peer-reviewed. Any opinions or recommendations discussed are solely those of the author(s) and are not endorsed by BMJ. BMJ disclaims all liability and responsibility arising from any reliance placed on the content. Where the content includes any translated material, BMJ does not warrant the accuracy and reliability of the translations (including but not limited to local regulations, clinical guidelines, terminology, drug names and drug dosages), and is not responsible for any error and/or omissions arising from translation and adaptation or otherwise.

Open access This is an open access article distributed in accordance with the Creative Commons Attribution Non Commercial (CC BY-NC 4.0) license, which permits others to distribute, remix, adapt, build upon this work non-commercially, and license their derivative works on different terms, provided the original work is

properly cited, appropriate credit is given, any changes made indicated, and the use is non-commercial. See: <http://creativecommons.org/licenses/by-nc/4.0/>.

ORCID iDs

Ruiyi Zhang <http://orcid.org/0000-0002-8184-8147>

Mengzhou Xue <http://orcid.org/0000-0002-2329-0050>

REFERENCES

- Cordonnier C, Demchuk A, Ziai W, et al. Intracerebral haemorrhage: current approaches to acute management. *Lancet* 2018;392:1257–68.
- van Asch CJ, Luitse MJ, Rinkel GJ, et al. Incidence, case fatality, and functional outcome of intracerebral haemorrhage over time, according to age, sex, and ethnic origin: a systematic review and meta-analysis. *Lancet Neurol* 2010;9:167–76.
- Zhang R, Xue M, Yong VW. Central nervous system tissue regeneration after intracerebral hemorrhage: the next frontier. *Cells* 2021;10:2513.
- Xue M, Yong VW. Neuroinflammation in intracerebral haemorrhage: immunotherapies with potential for translation. *Lancet Neurol* 2020;19:1023–32.
- Bai Q, Xue M, Yong VW. Microglia and macrophage phenotypes in intracerebral haemorrhage injury: therapeutic opportunities. *Brain* 2020;143:1297–314.
- Shtaya A, Bridges LR, Esiri MM, et al. Rapid neuroinflammatory changes in human acute intracerebral hemorrhage. *Ann Clin Transl Neurol* 2019;6:1465–79.
- Askenase MH, Goods BA, Beatty HE, et al. Longitudinal transcriptomics define the stages of myeloid activation in the living human brain after intracerebral hemorrhage. *Sci Immunol* 2021;6:eabd6279.
- Zhu H, Wang Z, Yu J, et al. Role and mechanisms of cytokines in the secondary brain injury after intracerebral hemorrhage. *Prog Neurobiol* 2019;178:101610.
- Mracsko E, Javidi E, Na S-Y, et al. Leukocyte invasion of the brain after experimental intracerebral hemorrhage in mice. *Stroke* 2014;45:2107–14.
- Hammond MD, Taylor RA, Mullen MT, et al. CCR2+ Ly6C (Hi) inflammatory monocyte recruitment exacerbates acute disability following intracerebral hemorrhage. *J Neurosci* 2014;34:3901–9.
- Chang C-F, Goods BA, Askenase MH, et al. Erythrocyte efferocytosis modulates macrophages towards recovery after intracerebral hemorrhage. *J Clin Invest* 2018;128:607–24.
- Yang Z, Zhong S, Liu Y, et al. Scavenger receptor SRA attenuates microglia activation and protects neuroinflammatory injury in intracerebral hemorrhage. *J Neuroimmunol* 2015;278:232–8.
- Wang B, Tontonoz P. Liver X receptors in lipid signalling and membrane homeostasis. *Nat Rev Endocrinol* 2018;14:452–63.
- Willy PJ, Umesono K, Ong ES, et al. Lxr, a nuclear receptor that defines a distinct retinoid response pathway. *Genes Dev* 1995;9:1033–45.
- Chen JD, Evans RM. A transcriptional co-repressor that interacts with nuclear hormone receptors. *Nature* 1995;377:454–7.
- Hörlein AJ, Näär AM, Heinzl T, et al. Ligand-independent repression by the thyroid hormone receptor mediated by a nuclear receptor co-repressor. *Nature* 1995;377:397–404.
- Skerrett R, Malm T, Landreth G. Nuclear receptors in neurodegenerative diseases. *Neurobiol Dis* 2014;72 Pt A:104–16.
- Hong C, Tontonoz P. Liver X receptors in lipid metabolism: opportunities for drug discovery. *Nat Rev Drug Discov* 2014;13:433–44.
- Janowski BA, Willy PJ, Devi TR, et al. An oxysterol signalling pathway mediated by the nuclear receptor LXR alpha. *Nature* 1996;383:728–31.
- Fu X, Menke JG, Chen Y, et al. 27-Hydroxycholesterol is an endogenous ligand for liver X receptor in cholesterol-loaded cells. *Journal of Biological Chemistry* 2001;276:38378–87.
- Lehmann JM, Kliewer SA, Moore LB, et al. Activation of the nuclear receptor LXR by oxysterols defines a new hormone response pathway. *J Biol Chem* 1997;272:3137–40.
- Wang M, Thomas J, Burris TP, et al. Molecular determinants of LXRalpha agonism. *J Mol Graph Model* 2003;22:173–81.
- Song C, Liao S. Hypolipidemic effects of selective liver X receptor alpha agonists. *Steroids* 2001;66:673–81.
- Färnegårdh M, Bonn T, Sun S, et al. The three-dimensional structure of the liver X receptor β reveals a flexible ligand-binding pocket that can accommodate fundamentally different ligands. *Journal of Biological Chemistry* 2003;278:38821–8.
- Theofilopoulos S, Wang Y, Kitambi SS, et al. Brain endogenous liver X receptor ligands selectively promote midbrain neurogenesis. *Nat Chem Biol* 2013;9:126–33.
- Glass CK, Rosenfeld MG. The coregulator exchange in transcriptional functions of nuclear receptors. *Genes Dev* 2000;14:121–41.
- Vitali C, Wellington CL, Calabresi L. Hdl and cholesterol handling in the brain. *Cardiovasc Res* 2014;103:405–13.
- Sun T, Li Y-J, Tian Q-Q, et al. Activation of liver X receptor β -enhancing neurogenesis ameliorates cognitive impairment induced by chronic cerebral hypoperfusion. *Exp Neurol* 2018;304:21–9.
- Berghoff SA, Spieth L, Sun T, et al. Microglia facilitate repair of demyelinated lesions via post-squalene sterol synthesis. *Nat Neurosci* 2021;24:47–60.
- Cantuti-Castelvetri L, Fitzner D, Bosch-Queralt M, et al. Defective cholesterol clearance limits remyelination in the aged central nervous system. *Science* 2018;359:684–8.
- Ghisletti S, Huang W, Ogawa S, et al. Parallel SUMOylation-dependent pathways mediate gene- and signal-specific transrepression by LXRs and PPARgamma. *Mol Cell* 2007;25:57–70.
- Lee JH, Park SM, Kim OS, et al. Differential sumoylation of LXRalpha and LXRbeta mediates transrepression of STAT1 inflammatory signaling in IFN-gamma-stimulated brain astrocytes. *Mol Cell* 2009;35:806–17.
- Saijo K, Crotti A, Glass CK. Regulation of microglia activation and deactivation by nuclear receptors. *Glia* 2013;61:104–11.
- Thomas DG, Doran AC, Fotakis P, et al. Lxr suppresses inflammatory gene expression and neutrophil migration through cis-repression and cholesterol efflux. *Cell Rep* 2018;25:3774–85.
- Bai Q, Sheng Z, Liu Y, et al. Intracerebral haemorrhage: from clinical settings to animal models. *Stroke Vasc Neurol* 2020;5:388–95.
- Cui X, Chopp M, Zhang Z, et al. ABCA1/ApoE/HDL pathway mediates GW3965-induced neurorestoration after stroke. *Stroke* 2017;48:459–67.
- Dong Y, Jain RW, Lozinski BM, et al. Single-Cell and spatial RNA sequencing identify perturbators of microglial functions with aging. *Nat Aging* 2022;2:508–25.
- Bosch-Queralt M, Cantuti-Castelvetri L, Damkou A, et al. Diet-Dependent regulation of TGF β impairs reparative innate immune responses after demyelination. *Nat Metab* 2021;3:211–27.
- Duewell P, Kono H, Rayner KJ, et al. Nlrp3 inflammasomes are required for atherogenesis and activated by cholesterol crystals. *Nature* 2010;464:1357–61.
- Hornung V, Bauernfeind F, Halle A, et al. Silica crystals and aluminum salts activate the NALP3 inflammasome through phagosomal destabilization. *Nat Immunol* 2008;9:847–56.
- Knight RA, Han Y, Nagaraja TN, et al. Temporal MRI assessment of intracerebral hemorrhage in rats. *Stroke* 2008;39:2596–602.
- Yang J, Li Q, Wang Z, et al. Multimodality MRI assessment of grey and white matter injury and blood-brain barrier disruption after intracerebral haemorrhage in mice. *Sci Rep* 2017;7:40358.
- Tofts PS, Brix G, Buckley DL, et al. Estimating kinetic parameters from dynamic contrast-enhanced T (1) -weighted MRI of a diffusable tracer: standardized quantities and symbols. *J Magn Reson Imaging* 1999;10:223–32.
- Tofts PS, Kermode AG. Measurement of the blood-brain barrier permeability and leakage space using dynamic MR imaging. 1. Fundamental concepts. *Magn Reson Med* 1991;17:357–67.
- Yeh FC, Liu L, Hitchens TK, et al. Mapping immune cell infiltration using restricted diffusion MRI. *Magn Reson Med* 2017;77:603–12.
- Yeh F-C, Wedeen VJ, Tseng W-YI. Generalized q-sampling imaging. *IEEE Trans Med Imaging* 2010;29:1626–35.
- Liu J, Li N, Zhu Z, et al. Vitamin D enhances hematoma clearance and neurologic recovery in intracerebral hemorrhage. *Stroke* 2022;53:2058–68.
- Jing C, Bian L, Wang M, et al. Enhancement of hematoma clearance with CD47 blocking antibody in experimental intracerebral hemorrhage. *Stroke* 2019;50:1539–47.
- Yong VW. Microglia in multiple sclerosis: protectors turn destroyers. *Neuron* 2022;110:3534–48.
- Chen Y, Popko B. Cholesterol crystals impede nerve repair. *Science* 2018;359:635–6.
- Yeh F-C, Verstynen TD, Wang Y, et al. Deterministic diffusion fiber tracking improved by quantitative anisotropy. *PLoS ONE* 2013;8:e80713.
- Zhang H, Wang Y, Lu T, et al. Differences between generalized q-sampling imaging and diffusion tensor imaging in the preoperative



- visualization of the nerve fiber tracts within peritumoral edema in brain. *Neurosurgery* 2013;73:1044–53.
- 53 Wu C-H, Chen C-C, Lai C-Y, *et al.* Treatment with TO901317, a synthetic liver X receptor agonist, reduces brain damage and attenuates neuroinflammation in experimental intracerebral hemorrhage. *J Neuroinflammation* 2016;13:62.
- 54 Cui X, Chopp M, Zacharek A, *et al.* The neurorestorative benefit of GW3965 treatment of stroke in mice. *Stroke* 2013;44:153–61.
- 55 Conti L, Cattaneo E. Controlling neural stem cell division within the adult subventricular zone: an appealing job. *Trends Neurosci* 2005;28:57–9.
- 56 Wang B, Wang Z, Sun L, *et al.* The amyloid precursor protein controls adult hippocampal neurogenesis through GABAergic interneurons. *J Neurosci* 2014;34:13314–25.
- 57 Caillé I, Allinquant B, Dupont E, *et al.* Soluble form of amyloid precursor protein regulates proliferation of progenitors in the adult subventricular zone. *Development* 2004;131:2173–81.
- 58 Nugent AA, Lin K, van Lengerich B, *et al.* Trem2 regulates microglial cholesterol metabolism upon chronic phagocytic challenge. *Neuron* 2020;105:837–54.
- 59 Groot PHE, Pearce NJ, Yates JW, *et al.* Synthetic LXR agonists increase LDL in CETP species. *Journal of Lipid Research* 2005;46:2182–91.
- 60 Schultz JR, Tu H, Luk A, *et al.* Role of LXRs in control of lipogenesis. *Genes Dev* 2000;14:2831–8.
- 61 Joseph SB, Laffitte BA, Patel PH, *et al.* Direct and indirect mechanisms for regulation of fatty acid synthase gene expression by liver X receptors. *Journal of Biological Chemistry* 2002;277:11019–25.
- 62 Katz A, Udata C, Ott E, *et al.* Safety, pharmacokinetics, and pharmacodynamics of single doses of LXR-623, a novel liver X-receptor agonist, in healthy participants. *J Clin Pharmacol* 2009;49:643–9.
- 63 Lund EG, Peterson LB, Adams AD, *et al.* Different roles of liver X receptor alpha and beta in lipid metabolism: effects of an alpha-selective and a dual agonist in mice deficient in each subtype. *Biochem Pharmacol* 2006;71:453–63.
- 64 Quinet EM, Savio DA, Halpern AR, *et al.* Liver X receptor (LXR)-beta regulation in Lxralpha-deficient mice: implications for therapeutic targeting. *Mol Pharmacol* 2006;70:1340–9.